Dyadic Green's functions of thin films: Applications within plasmonic solar cells

Jesper Jung,[1,2,*] Thomas Søndergaard,[1] Thomas Garm Pedersen,[1,2] Kjeld Pedersen,[1,2]
Arne Nylandsted Larsen,[3,2] and Brian Bech Nielsen[3,2]

[1]*Department of Physics and Nanotechnology, Aalborg University, Skjernvej 4A, DK-9220 Aalborg Øst, Denmark*
[2]*Interdisciplinary Nanoscience Center (iNANO), Denmark*
[3]*Department of Physics and Astronomy, Aarhus University, DK-8000 Aarhus C, Denmark*

Optimization and design of silicon solar cells by exploiting light scattering from metal nanoparticles to increase the efficiency is addressed in the small particle limit from a fundamental point of view via the dyadic Green's function formulation. Based on the dyadic Green's function (Green's tensor) of a three-layer geometry, light scattering from electric point dipoles (representing small metal scatterers) located within a thin layer sandwiched between a substrate and a superstrate is analyzed. Starting from the full dyadic Green's function we derive analytical near- and far-field approximations. The far-field approximations enable efficient, exact, and separate evaluation of light scattering into waves that propagate in the substrate or the superstrate. Based on the near-field approximation we present a semianalytical expression for the total near-field absorption in the substrate. The theoretical approach is used to analyze realistic configurations for plasmon-assisted silicon solar cells. We show that by embedding metal nanoscatterers in a thin film with a high refractive index (rutile TiO_2 with $n \approx 2.5$) on top of the silicon, the fraction of scattered light that couples into the solar cell can become larger than 96%, and an optical path length enhancement of more than 100 can be achieved.

I. INTRODUCTION

Collective excitations of the free conduction electrons in metal nanoparticles can be resonantly excited with light.[1–4] Such excitations are termed *particle plasmons* or *localized surface plasmons* and have recently shown promise in the development of thin-film silicon solar cells.[5] At a plasmon resonance frequency a metal nanoparticle can become a strong scatterer of light, displaying a scattering cross section that even exceeds its geometrical cross section. This is utilized in plasmon-assisted silicon solar cells, where the strong scattering capabilities of nearby metal nanoparticles are used to scatter the incident solar radiation in order to increase the optical path length and hence the absorption of light within the silicon layer.[6,7] Efficient thin-film solar cells are crucial for the commercial success of silicon-based photovoltaics as the material cost of the thick silicon layer required in order to absorb the long-wavelength part of the Sun's spectrum is a serious obstacle for present day silicon solar cells when compared to other energy technologies.

Light trapping via particle plasmons of metal nanoparticles was sparked by Stuart and Hall in 1996, when they measured absorption enhancement in silicon-on-insulator waveguides using metal island films,[8] and later in 1998, when they studied metal nanoparticle size effects in plasmon-enhanced photodetectors.[9] Following their pioneering work there have recently been several experimental demonstrations of enhanced optical absorption in semiconductors using metal nanoparticles; see, for example, Refs. 10–13. Theoretically, however, the subject has not been much studied, but it is well known that if a metal nanoparticle is small compared to the wavelength, the scattered radiation is dipole-like. Thus, in a homogenous surrounding the radiation pattern is highly symmetric.[14] However, if the metal nanoparticle is placed within close proximity of an interface, the situation changes and a strong directional scattering into the material with the highest refractive index can be observed.[15] In Refs. 6 and 7, the

influence of size and shape of metal nanoparticles close to a silicon surface on scattering cross section, coupling efficiency, and path length enhancement has been studied using brute force finite-difference time-domain (FDTD)[16] calculations. In general, FDTD approaches are not practical in open infinite-scattering problems involving metal nanoparticles because the entire computational domain must be discretized and a detailed mesh near metal edges is necessary. Furthermore, a finite-size computational window must be introduced. As a consequence, FDTD calculations often become tedious and time-consuming, in particular when different parameters of the configuration must be swept in the analysis.

To gain physical insight into directional scattering from metal nanoparticles in layered geometries we wish to analyze the problem, in the small particle limit, from a fundamental theoretical point of view. Our starting point is the Green's dyadic formulation for stratified media,[17–25] where we, in particular, are interested in the configuration where the metal scatterer is located within a thin film sandwiched between one substrate and one superstrate medium. In the previous work of Refs. 6 and 7 the scattering analysis was performed for nanoparticles placed on top of the silicon surface. Here we suggest a configuration where the metal scatterer is embedded in a high refractive index film on top of the silicon. Beside being more practical in a realistic solar cell design, this approach has two important advantages. First, the high refractive index of the film will shift the particle plasmon resonances toward near-infrared wavelengths where silicon is a poor light absorber. Second, by lowering the index contrast at the silicon interface, scattered light will be able to couple into the silicon under larger angles and the maximum allowed angle will increase. This is important because larger refraction angles are directly related to larger optical path lengths within the silicon layer.

We have previously shown how the induced dipole moment of a small (with respect to the wavelength) metal nanoparticle

within a thin film can be obtained by solving an electrostatic Green's function surface integral equation for the surface polarization charge density.[26,27] In this work we study the dyadic Green's function (including all retardation effects) and its near- and far-field approximations for such a dipole emitter. We show *inter alia* how the far-field approximations can be used for efficient and exact semianalytical evaluation of light scattering both into the substrate and the superstrate. As we show in the following section, when the induced dipole moment of a small metal particle is known the scattered radiation can be obtained via the dyadic Green's function of the reference structure. Radiation from an electric dipole within a layered geometry has to some extent been studied before using the Hertz vector formalism,[28,29] however, not in the context of plasmonic solar cells. It should be noted that the dyadic Green's function of the present work can directly be utilized in conjunction with well-known Green's function volume, or surface, integral equation methods (see, for example, Refs. 30–35), for example, in an electrodynamical scattering analysis of an arbitrarily shaped metal nanoparticle within a layered geometry. Exact scattering analysis of such a configuration could be very important for the development of plasmon-assisted solar cells.

The paper is organized as follows. In Sec. II we present the theoretical foundation of our scattering analysis. Starting from the dyadic Green's function we derive its far-field approximations and we present scattering cross sections for light scattered into the substrate and into the superstrate. Thereafter near-field approximations and absorption in the substrate is presented. In Sec. III we utilize the derived theory to analyze directional light scattering for a dipole emitter within a thin layer in the context of plasmon-assisted silicon solar cells. In Sec. IV we present our conclusions and in the appendixes, additional calculations supporting Sec. II can be found.

II. THEORY

In the scattering analysis we start by assuming that the metal scatterer embedded within the film is small compared to the wavelength. In the small particle limit it is widely known that a metal particle scatters light like an electric point dipole radiates. Thus, it can easily be shown that the scattered electric field from the particle can be calculated as[21]

$$\mathbf{E}_s(\mathbf{r}) = \omega^2 \mu_0 \mathbf{G}(\mathbf{r},\mathbf{r}_0) \cdot \mathbf{p}_0, \tag{1}$$

where $\mathbf{p}_0$ is the induced dipole moment at the position $\mathbf{r}_0$, ω is the angular frequency where we have assumed time harmonic fields as $E \propto \exp(-i\omega t)$, μ_0 is the magnetic vacuum permeability, and $\mathbf{G}(\mathbf{r},\mathbf{r}')$ is the dyadic Green's function defined by

$$\nabla \times \nabla \times \mathbf{G}(\mathbf{r},\mathbf{r}') - k_0^2 \varepsilon_{\text{ref}}(\mathbf{r})\mathbf{G}(\mathbf{r},\mathbf{r}') = \mathbf{U}\delta(\mathbf{r} - \mathbf{r}'), \tag{2}$$
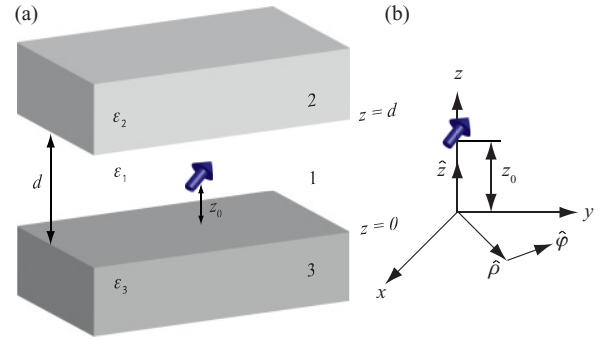
FIG. 1. (Color online) (a) Dipole emitter between a substrate (medium 3) and a superstrate (medium 2). The dielectric constants of the substrate, the film, and the superstrate are all assumed frequency independent and are given by ε_3, ε_1, and ε_2, respectively. (b) Coordinate system defining the cylindrical unit vectors $\hat{z}$, $\hat{\rho}$, and $\hat{\varphi}$.

with $\mathbf{U}$ the unit dyadic, k_0 the vacuum wave number, and where it is required that $\mathbf{G}(\mathbf{r},\mathbf{r}')$ fulfills the radiation boundary condition. Thus if the induced dipole moment is known the scattered (or radiated) electric field $\mathbf{E}_s(\mathbf{r})$ can easily be calculated via the dyadic Green's function.

We start our analysis by choosing the center of the scatterer as $\mathbf{r}' = \mathbf{r}_0 = z_0\hat{z}$, a coordinate system such that the two interfaces are in the xy plane at $z = 0$ and $z = d$, and z_0 such that $0 < z_0 < d$ (Fig. 1). To calculate the scattered part of the electric field in the super- and substrate we used the dyadic Green's functions $\mathbf{G}_2(\mathbf{r},\mathbf{r}')$ and $\mathbf{G}_3(\mathbf{r},\mathbf{r}')$ for $\mathbf{r} > d$ and $\mathbf{r} < 0$, respectively. These can be constructed by following the procedure described in Refs. 17, 18, 20, 22, and 23. Note, however, as pointed out in Ref. 22, that the formulation in the review article of Ref. 18 from 1978 is incorrect as the wave vector eigenfunctions used are incomplete. In the following three sections we present the dyadic Green's functions $\mathbf{G}_2(\mathbf{r},\mathbf{r}')$ and $\mathbf{G}_3(\mathbf{r},\mathbf{r}')$, we derive their far-field approximations, and we present the scattering cross sections for light scattered into the substrate and into the superstrate. We have derived the far-field approximations of the dyadic Green's functions from two different approaches. In the first approach we start from the foundation of Ref. 22, and in the second approach, which we present in Appendix B, we start out with the dyadic Green's function of a homogenous medium and construct $\mathbf{G}_2(\mathbf{r},\mathbf{r}')$ and $\mathbf{G}_3(\mathbf{r},\mathbf{r}')$ by taking into account all the multiple reflections within the three-layer reference structure.

A. The dyadic Green's functions

Following Ref. 22, $\mathbf{G}_2(\mathbf{r},\mathbf{r}')$ and $\mathbf{G}_3(\mathbf{r},\mathbf{r}')$ may be expressed as

$$\mathbf{G}_2(\mathbf{r},\mathbf{r}') = \frac{i}{4\pi} \int_0^\infty \frac{d\kappa_\rho}{\kappa_\rho \kappa_{z_1}} \sum_{n=0}^\infty \sum_{j=0}^1 g_n \frac{e^{i\kappa_{z_1}d}}{e^{i\kappa_{z_2}d}} \left[\frac{\left(1 + r_{12}^{(s)}\right)\mathbf{M}(\kappa_{z_2})\left(\mathbf{M}'_- + r_{13}^{(s)}\mathbf{M}'_+\right)}{1 - \eta r_{12}^{(s)} r_{13}^{(s)}} + \frac{k_1}{k_2} \frac{\left(1 + r_{12}^{(p)}\right)\mathbf{N}(\kappa_{z_2})\left(\mathbf{N}'_- + r_{13}^{(p)}\mathbf{N}'_+\right)}{1 - \eta r_{12}^{(p)} r_{13}^{(p)}} \right],$$

$$\mathbf{G}_3(\mathbf{r},\mathbf{r}') = \frac{i}{4\pi} \int_0^\infty \frac{d\kappa_\rho}{\kappa_\rho \kappa_{z_1}} \sum_{n=0}^\infty \sum_{j=0}^1 g_n \left[\frac{\left(1 + r_{13}^{(s)}\right)\mathbf{M}(-\kappa_{z_3})\left(\mathbf{M}'_+ + \eta r_{12}^{(s)}\mathbf{M}'_-\right)}{1 - \eta r_{12}^{(s)} r_{13}^{(s)}} + \frac{k_1}{k_3} \frac{\left(1 + r_{13}^{(p)}\right)\mathbf{N}(-\kappa_{z_3})\left(\mathbf{N}'_+ + \eta r_{12}^{(p)}\mathbf{N}'_-\right)}{1 - \eta r_{12}^{(p)} r_{13}^{(p)}} \right]. \tag{3}$$

Here, d is the thickness of the film, $\eta = e^{2i\kappa_{z_1}d}$, $k_i = \sqrt{\varepsilon_i}k_0$, $\kappa_{z_i} = \sqrt{k_i^2 - \kappa_\rho^2}$, $g_n = 2 - \delta_{n0}$, $\mathbf{N}_\pm = \mathbf{N}_{jn\kappa_\rho}(\pm\kappa_{z_1})$, $\mathbf{M}_\pm = \mathbf{M}_{jn\kappa_\rho}(\pm\kappa_{z_1})$, where $k_0 = 2\pi/\lambda$, δ_{n0} is the Kronecker delta, and the cylindrical vector harmonics $\mathbf{N}_{jn\kappa_\rho}(\kappa_{z_i})$ and $\mathbf{M}_{jn\kappa_\rho}(\kappa_{z_1})$ are given as

$$\mathbf{N}_{jn\kappa_\rho}(\kappa_{z_i}) = \frac{e^{i\kappa_{z_i}z}}{k_i}\left[i\kappa_{z_i}\frac{\partial J_n(\kappa_\rho\rho)}{\partial\rho}\cos\left(j\frac{\pi}{2} - n\varphi\right)\hat{\rho} + i\kappa_{z_i}\frac{nJ_n(\kappa_\rho\rho)}{\rho}\sin\left(j\frac{\pi}{2} - n\varphi\right)\hat{\varphi} + \kappa_\rho^2 J_n(\kappa_\rho\rho)\cos\left(j\frac{\pi}{2} - n\varphi\right)\hat{z}\right],$$

$$\mathbf{M}_{jn\kappa_\rho}(\kappa_{z_i}) = e^{i\kappa_{z_i}z}\left[\frac{nJ_n(\kappa_\rho\rho)}{\rho}\sin\left(j\frac{\pi}{2} - n\varphi\right)\hat{\rho} - \frac{\partial J_n(\kappa_\rho\rho)}{\partial\rho}\cos\left(j\frac{\pi}{2} - n\varphi\right)\hat{\varphi}\right], \tag{4}$$

where J_n is the nth-order Bessel function of the first kind. In Eq. (3) the prime on the vector harmonics is used to indicate that they are expressed in terms of the coordinates (ρ', φ', z'), and $r_{1i}^{(s)}$ and $r_{1i}^{(p)}$ are the Fresnel reflection coefficients for s and p polarization given as

$$r_{1i}^{(s)} = \frac{\kappa_{z_1} - \kappa_{z_i}}{\kappa_{z_1} + \kappa_{z_i}},$$

$$r_{1i}^{(p)} = \frac{\varepsilon_i\kappa_{z_1} - \varepsilon_1\kappa_{z_i}}{\varepsilon_i\kappa_{z_1} + \varepsilon_1\kappa_{z_i}}, \tag{5}$$

such that the transmission coefficients become $t_{1i}^{(s)} = 1 + r_{1i}^{(s)}$ and $t_{1i}^{(p)} = 1 + r_{1i}^{(p)}$.

In the case of Fig. 1, where $\mathbf{r}' = \mathbf{r}_0 = z_0\hat{z}$, we have $\rho' = 0$ and $z' = z_0$. Hence, it is easy to show that the only surviving

primed cylindrical vector harmonics are

$$\mathbf{M}'_{01\kappa_\rho}(\kappa_{z_1}) = -\frac{\kappa_\rho}{2}e^{i\kappa_{z_1}z_0}[\sin\varphi'\hat{\rho}' + \cos\varphi'\hat{\varphi}'],$$

$$\mathbf{M}'_{11\kappa_\rho}(\kappa_{z_1}) = \frac{\kappa_\rho}{2}e^{i\kappa_{z_1}z_0}[\cos\varphi'\hat{\rho}' - \sin\varphi'\hat{\varphi}'],$$

$$\mathbf{N}'_{00\kappa_\rho}(\kappa_{z_1}) = \frac{\kappa_\rho^2}{k_1}e^{i\kappa_{z_1}z_0}\hat{z}', \tag{6}$$

$$\mathbf{N}'_{01\kappa_\rho}(\kappa_{z_1}) = i\frac{\kappa_\rho\kappa_{z_1}}{2k_1}e^{i\kappa_{z_1}z_0}[\cos\varphi'\hat{\rho}' - \sin\varphi'\hat{\varphi}'],$$

$$\mathbf{N}'_{11\kappa_\rho}(\kappa_{z_1}) = i\frac{\kappa_\rho\kappa_{z_1}}{2k_1}e^{i\kappa_{z_1}z_0}[\sin\varphi'\hat{\rho}' + \cos\varphi'\hat{\varphi}'].$$

By using Eq. (6) in Eq. (3) and by splitting the dyadic Green's function into s- and p-polarized contributions as $\mathbf{G}_i(\mathbf{r},\mathbf{r}') = \mathbf{G}_i^{(s)}(\mathbf{r},\mathbf{r}') + \mathbf{G}_i^{(p)}(\mathbf{r},\mathbf{r}')$ we obtain after some algebra,

$$\mathbf{G}_i^{(s)}(\mathbf{r},\mathbf{r}_0) = \frac{-i}{4\pi}\int_0^\infty d\kappa_\rho\frac{e^{\pm i\kappa_{z_i}z}}{\kappa_{z_1}}\xi_{+,i}^{(s)}(\kappa_\rho,z_0,d)\left[\frac{J_0'(\kappa_\rho\rho)}{\rho}\hat{\rho}\hat{\rho} + \kappa_\rho J_0''(\kappa_\rho\rho)\hat{\varphi}\hat{\varphi}\right], \tag{7a}$$

$$\mathbf{G}_i^{(p)}(\mathbf{r},\mathbf{r}_0) = \frac{i}{4\pi k_i^2}\int_0^\infty d\kappa_\rho e^{\pm i\kappa_{z_i}z}\left\{\xi_{+,i}^{(p)}(\kappa_\rho,z_0,d)\left[\frac{\kappa_\rho^3}{\kappa_{z_1}}J_0(\kappa_\rho\rho)\hat{z}\hat{z} \pm i\frac{\kappa_\rho^2\kappa_{z_i}}{\kappa_{z_1}}J_0'(\kappa_\rho\rho)\hat{\rho}\hat{z}\right]\right.$$

$$\left. + \xi_{-,i}^{(p)}(\kappa_\rho,z_0,d)\left[-\kappa_{z_i}\kappa_\rho J_0''(\kappa_\rho\rho)\hat{\rho}\hat{\rho} - \kappa_{z_i}\frac{J_0'(\kappa_\rho\rho)}{\rho}\hat{\varphi}\hat{\varphi} \pm i\kappa_\rho^2 J_0'(\kappa_\rho\rho)\hat{z}\hat{\rho}\right]\right\}, \tag{7b}$$

where the primes on the Bessel functions mean derivative with respect to the argument, the subscript i is 2 and $+$ is used if $\mathbf{r}$ is in the superstrate, and the subscript is 3 and $-$ is used if $\mathbf{r}$ is in the substrate. In addition, the factors $\xi_{\pm,i}^{(x)}(\kappa_\rho,z_0,d)$ are given as

$$\xi_{\pm,2}^{(x)}(\kappa_\rho,z_0,d) = \frac{t_{12}^{(x)}\left[e^{i\kappa_{z_1}(d-z_0)} \pm r_{13}^{(x)}e^{i\kappa_{z_1}(d+z_0)}\right]}{1 - r_{12}^{(x)}r_{13}^{(x)}e^{2i\kappa_{z_1}d}}e^{-i\kappa_{z_2}d},$$

$$\xi_{\pm,3}^{(x)}(\kappa_\rho,z_0,d) = \frac{t_{13}^{(x)}\left[e^{i\kappa_{z_1}z_0} \pm r_{12}^{(x)}e^{i\kappa_{z_1}(2d-z_0)}\right]}{1 - r_{12}^{(x)}r_{13}^{(x)}e^{2i\kappa_{z_1}d}}, \tag{8}$$

where the superscript (x) is either (s) or (p) depending on the polarization. Equations (7) and (8) represent the full dyadic Green's functions with $\mathbf{r}$ in medium 2 and 3 for a dipole emitter located at $\mathbf{r}' = \mathbf{r}_0 = z_0\hat{z}$ in medium 1.

B. Far-field approximations

The propagators above include near-field contributions and in principle allow for lossy materials characterized by complex dielectric constants. In the present work, however, the materials can be considered lossless except for the silicon substrate. In fact, even in silicon the penetration depth is much greater than the wavelength in the range $\lambda > 700$ nm, which is the important one for plasmonic solar cells (see Sec. III) as shorter wavelength light typically is absorbed without assistance of plasmonic scatterers. Hence, in order to calculate the total intensity radiated into the substrate we utilize the usual far-field approach, where we neglect the small losses in the silicon. Eventually it is, of course, the losses in the silicon that are responsible for the absorption of light. However, given the fraction of light that radiates into the silicon substrate and the radiation pattern it is possible to estimate an optical path length enhancement factor $L_{\max}$, which specifies how much the optical path length within the silicon layer is enhanced due to the presence of metal nanoscatterers. Given $L_{\max}$ the maximum optical path length within a thin silicon film of a plasmon-assisted solar cell can be compared to the penetration depth of light in silicon. This analysis is made in the Results section (Sec. III). However, in order to estimate the

fraction of light that is scattered into the silicon the far-field approximations of the propagators and the scattering cross sections must be derived first.

In the far field, where ρ and z are large, we may approximate the cylindrical vector harmonics by making an asymptotic expansion of the Bessel functions as

$$\mathbf{M}_{jn\kappa_\rho}(\kappa_{z_i}) \approx e^{i\kappa_{z_i}z}\sqrt{\frac{2\kappa_\rho}{\pi\rho}}\sin\left(\kappa_\rho\rho - n\frac{\pi}{2} - \frac{\pi}{4}\right)$$
$$\times \cos\left(j\frac{\pi}{2} - n\varphi\right)\hat{\varphi}, \qquad (9)$$

$$\mathbf{N}_{jn\kappa_\rho}(\kappa_{z_i}) \approx \frac{e^{i\kappa_{z_i}z}}{k_i}\sqrt{\frac{2\kappa_\rho}{\pi\rho}}\left[\kappa_\rho\cos\left(\kappa_\rho\rho - n\frac{\pi}{2} - \frac{\pi}{4}\right)\hat{z}\right.$$
$$\left. - i\kappa_{z_i}\sin\left(\kappa_\rho\rho - n\frac{\pi}{2} - \frac{\pi}{4}\right)\hat{\rho}\right]\cos\left(j\frac{\pi}{2} - n\varphi\right),$$

and the κ_ρ integration limit can be taken as k_i because only the propagating waves are important. This allows us to set $\kappa_\rho = k_i\sin\alpha$ which yields $\kappa_{z_i} = k_i\cos\alpha$ and $d\kappa_\rho = \kappa_{z_i}d\alpha$. Furthermore we may introduce the refraction angle for the two interfaces 1-2 and 1-3 via $k_i\sin\alpha = k_1\sin\alpha'$ which yields $\kappa_{z_1} = k_1\cos\alpha'$. If we also introduce the angle θ (see Fig. 2) we get $z = -r\cos\theta$ and $\rho = r\sin\theta$ in the substrate and $z = r\cos\theta$ and $\rho = r\sin\theta$ in the superstrate. Using this together with Eqs. (6) and (9) in Eq. (3) is it easy to see that the integrand will contain exponentials such as

$$\exp\left(i\kappa_{z_i}|z| \pm i\kappa_\rho\rho\right) = \exp[ik_i r\cos(\alpha \mp \theta)]. \qquad (10)$$
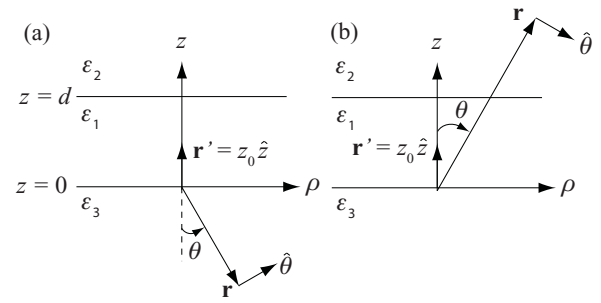
FIG. 2. $z\rho$ plane defining θ and $\hat{\theta}$ (a) for $\mathbf{r}$ in the substrate, and (b) for $\mathbf{r}$ in the superstrate.

Hence we need to evaluate integrals like

$$\int_0^{\pi/2} d\alpha f(\alpha)\exp[ik_i r\cos(\alpha \mp \theta)], \qquad (11)$$

where $f(\alpha)$ is a complicated function of the angle α. In the far-field limit the integral with $\cos(\alpha + \theta)$ vanishes and the other yields (see Appendix A)

$$f(\theta)\sqrt{\frac{2\pi}{ik_i r}}e^{ik_i r}. \qquad (12)$$

Using this, the far-field approximations of the full dyadic Green's functions in Eq. (7) can be obtained after some algebra. For the superstrate we obtain the following far-field approximation, where κ_ρ now is a function of θ:

$$\mathbf{G}_2^{(\text{ff})}(\mathbf{r},\mathbf{r}_0) = \frac{e^{ik_2 r}}{4\pi r}\left[\frac{\kappa_{z_2}}{\kappa_{z_1}}\xi_{+,2}^{(s)}(\theta,z_0,d)\hat{\varphi}\hat{\varphi} - \sin\theta\frac{\kappa_{z_2}}{\kappa_{z_1}}\xi_{+,2}^{(p)}(\theta,z_0,d)\hat{\theta}\hat{z} + \cos\theta\xi_{-,2}^{(p)}(\theta,z_0,d)\hat{\theta}\hat{\rho}\right], \qquad (13)$$

where $\hat{\theta} = -\sin\theta\hat{z} + \cos\theta\hat{\rho}$ [see Fig. 2(b)], and it is understood that now $\kappa_{z_2} = k_2\cos\theta$, $\kappa_{z_1} = k_1\sqrt{1 - \sin^2\theta\,\varepsilon_2/\varepsilon_1}$, and $\kappa_{z_3} = k_3\sqrt{1 - \sin^2\theta\,\varepsilon_2/\varepsilon_3}$. For the substrate we obtain

$$\mathbf{G}_3^{(\text{ff})}(\mathbf{r},\mathbf{r}_0) = \frac{e^{ik_3 r}}{4\pi r}\left[\frac{\kappa_{z_3}}{\kappa_{z_1}}\xi_{+,3}^{(s)}(\theta,z_0,d)\hat{\varphi}\hat{\varphi} + \sin\theta\frac{\kappa_{z_3}}{\kappa_{z_1}}\xi_{+,3}^{(p)}(\theta,z_0,d)\hat{\theta}\hat{z} + \cos\theta\xi_{-,3}^{(p)}(\theta,z_0,d)\hat{\theta}\hat{\rho}\right], \qquad (14)$$

where now $\hat{\theta} = \sin\theta\hat{z} + \cos\theta\hat{\rho}$ [see Fig. 2(a)], $\kappa_{z_3} = k_3\cos\theta$, $\kappa_{z_1} = k_1\sqrt{1 - \sin^2\theta\,\varepsilon_3/\varepsilon_1}$, and $\kappa_{z_2} = k_2\sqrt{1 - \sin^2\theta\,\varepsilon_3/\varepsilon_2}$.

C. Scattering cross sections

To evaluate light scattering (or dipole radiation) into the substrate and the superstrate separately two scattering cross sections are defined: one where we integrate the flux of the radiation over a semisphere of infinite radius in the superstrate $\sigma_2(\omega)$, and a second where we integrate the flux over a corresponding semisphere in the substrate $\sigma_3(\omega)$. Note that because we consider radiation from a point dipole, with no physical size, which really acts as a radiator and not a scatterer, the term "scattering cross section" can seem a bit strange. However, because the point dipole here is used to model a small metal scatterer we choose the term scattering cross section for

the integrated flux of the radiation from the point dipole. The flux of the radiation corresponds to the time-averaged Poynting vector $\langle\mathbf{S}_s\rangle$. To obtain scattering cross sections similar to what is else found in the literature we normalize the integrated time-averaged Poynting vector with the magnitude of the Poynting vector $|\mathbf{S}_0|$ of a plane wave in medium 1. However, in what follows it is not important how the scattering cross section is normalized because we are interested in the ratio between light scattered into the substrate and into the superstrate. The scattering cross section is calculated as

$$\sigma_i(\omega) = \frac{\int_0^{2\pi}\int_0^{\frac{\pi}{2}}\sin\theta d\theta d\varphi\langle\mathbf{S}_s\rangle\cdot\hat{r}r^2}{|\mathbf{S}_0|} \qquad (15)$$

with $\langle\mathbf{S}_s\rangle = \frac{1}{2}\text{Re}\{\mathbf{E}_s \times \mathbf{H}_s^*\}$ and $|\mathbf{S}_0| = \frac{1}{2}\epsilon_0 c\sqrt{\varepsilon_1}|\mathbf{E}_0|^2$, where we have assumed that ε_1 is real. If we consider scattering into the substrate the subscript i is 3 and the θ angle is defined

as shown in Fig. 2(a), whereas if we consider scattering into the superstrate $i = 2$ and θ is defined by Fig. 2(b). To calculate the time-averaged Poynting vector both the scattered electric and magnetic field must be calculated. We calculate the scattered electric field from Eq. (1) using the far-field approximations of the dyadic Green's functions in Eqs. (13) and (14). The scattered magnetic field is then afterwards found using the Maxwell equation $\nabla \times \mathbf{E} = -\frac{\partial}{\partial t}\mathbf{B}$ which

yields

$$\mathbf{H}_s = \frac{-i}{\omega\mu_0}\nabla \times \mathbf{E}_s \approx \frac{k_i}{\omega\mu_0}\hat{r} \times \mathbf{E}_s, \qquad (16)$$

where we have used the far-field approximation that $\nabla(\frac{\exp(ik_ir)}{r})\times \approx ik_i\frac{\exp(ik_ir)}{r}\hat{r}\times$. Using this the scattering cross sections from a vertical dipole emitter $\mathbf{p}_0 = p_0\hat{z}$ in the sub- and superstrate (subscript i is either 2 or 3, respectively) becomes

$$\sigma_i^{(v)}(\omega,z_0,d) = \frac{k_0^4|p_0|^2}{16\pi^2\epsilon_0^2|E_0|^2}\sqrt{\frac{\varepsilon_i}{\varepsilon_1}}\int_0^{2\pi}\int_0^{\frac{\pi}{2}}\sin\theta d\theta d\varphi \left|\frac{\kappa_{z_i}}{\kappa_{z_1}}\xi_{+,i}^{(p)}(\theta,z_0,d)\right|^2\sin^2\theta, \qquad (17)$$

where the superscript v is used for vertical dipoles. Note that the φ integration simply yields 2π. For a horizontal dipole, for example, $\mathbf{p}_0 = p_0\hat{x}$ the scattering cross section becomes

$$\sigma_i^{(h)}(\omega,z_0,d) = \frac{k_0^4|p_0|^2}{16\pi^2\epsilon_0^2|E_0|^2}\sqrt{\frac{\varepsilon_i}{\varepsilon_1}}\int_0^{2\pi}\int_0^{\frac{\pi}{2}}\sin\theta d\theta d\varphi \left\{\left|\frac{\kappa_{z_i}}{\kappa_{z_1}}\xi_{+,i}^{(s)}(\theta,z_0,d)\right|^2\sin^2\varphi + \left|\xi_{-,i}^{(p)}(\theta,z_0,d)\right|^2\cos^2\varphi\cos^2\theta\right\}, \qquad (18)$$

where the superscript h is used for horizontal dipoles and the integration over φ yields a factor of π.

D. Near-field approximation and absorption in the substrate

In this section we utilize the dyadic Green's function formalism to study in detail near-field absorption in the substrate. We are interested in the absorption in the silicon substrate in the volume schematically illustrated by the gray shading in Fig. 3. The analysis is performed by making a near-field approximation of the dyadic Green's function $\mathbf{G}_3(\mathbf{r},\mathbf{r}_0)$. Given the near-field dyadic Green's function both the near field and its absorption can be evaluated.

In the near field we disregard all retardation effects, hence we take the limit where the speed of light approaches infinity, $c \to \infty$. Thus $\kappa_{z_i} = \sqrt{k_i^2 - \kappa_\rho^2} \to i\kappa_\rho$ and

$$r_{1i}^s = \frac{\kappa_{z_1} - \kappa_{z_i}}{\kappa_{z_1} + \kappa_{z_i}} \to 0,$$

$$r_{1i}^p = \frac{\varepsilon_i\kappa_{z_1} - \varepsilon_1\kappa_{z_i}}{\varepsilon_i\kappa_{z_1} + \varepsilon_1\kappa_{z_i}} \to \frac{\varepsilon_i - \varepsilon_1}{\varepsilon_i + \varepsilon_1} \equiv -\beta_i, \qquad (19)$$

where β_i is the "electrostatic" reflection coefficient introduced previously in the image charge description of plasmon

resonances.[26] Utilizing this the near-field approximation of the dyadic Green's function $\mathbf{G}_3(\mathbf{r},\mathbf{r}_0)$ becomes

$$\mathbf{G}_3^{\mathrm{nf}}(\mathbf{r},\mathbf{r}_0)$$
$$= \frac{1}{4\pi k_3^2}\int_0^\infty d\kappa_\rho\kappa_\rho^2 e^{\kappa_\rho z}\left\{\xi_{+,3}^{(p)}[J_0(\kappa_\rho\rho)\hat{z}\hat{z} + J_0'(\kappa_\rho\rho)\hat{\rho}\hat{z}]\right.$$
$$\left. + \xi_{-,3}^{(p)}\left[J_0''(\kappa_\rho\rho)\hat{\rho}\hat{\rho} + \frac{J_0'(\kappa_\rho\rho)}{\kappa_\rho\rho}\hat{\varphi}\hat{\varphi} + J_0'(\kappa_\rho\rho)\hat{z}\hat{\rho}\right]\right\} \quad (20)$$

with

$$\xi_{\pm,3}^{(p)} = (1 - \beta_3)\frac{e^{-\kappa_\rho z_0} \mp \beta_2 e^{-\kappa_\rho(2d-z_0)}}{1 - \beta_2\beta_3 e^{-2\kappa_\rho d}}$$

$$= (1 - \beta_3)(e^{-\kappa_\rho z_0} \mp \beta_2 e^{-\kappa_\rho(2d-z_0)})\sum_{n=0}^\infty(\beta_2\beta_3)^n e^{-2\kappa_\rho nd}, \qquad (21)$$

where the geometrical series for all the multiple reflections in $\xi_{\pm,3}^{(p)}$ has been unfolded. By doing this, the κ_ρ integral in Eq. (20) can be performed analytically. Note that the near-field dyadic Green's function only contains p-polarized contributions. In fact, an s-polarized contribution to the dyadic Green's function also exists for $c \to \infty$; however, this part is disregarded, as it is not a true near-field term because it only decays as $1/r$ and not $1/r^3$. Furthermore there is no s-polarized contribution to the near-field obtained after using Eq. (1) if $c \to \infty$. By introducing the four integrals

$$\Gamma_1(\rho,z) = \int_0^\infty d\kappa_\rho\kappa_\rho^2 e^{-\kappa_\rho z}J_0(\kappa_\rho\rho) = \frac{2z^2 - \rho^2}{(z^2 + \rho^2)^{5/2}},$$

$$\Gamma_2(\rho,z) = \int_0^\infty d\kappa_\rho\kappa_\rho^2 e^{-\kappa_\rho z}J_0'(\kappa_\rho\rho) = \frac{-3z\rho}{(z^2 + \rho^2)^{5/2}},$$

$$\Gamma_3(\rho,z) = \int_0^\infty d\kappa_\rho\kappa_\rho^2 e^{-\kappa_\rho z}J_0''(\kappa_\rho\rho) = \frac{2\rho^2 - z^2}{(z^2 + \rho^2)^{5/2}}, \qquad (22)$$

$$\Gamma_4(\rho,z) = \int_0^\infty d\kappa_\rho\kappa_\rho^2 e^{-\kappa_\rho z}\frac{J_0'(\kappa_\rho\rho)}{\kappa_\rho\rho} = -\frac{1}{(z^2 + \rho^2)^{3/2}},$$

FIG. 3. (Color online) Dipole emitter embedded in a film of thickness d. The distance from the substrate to the emitter is z_0. The gray shading illustrates where the near-field radiation of the dipole emitter primarily will be absorbed.

and the coordinates $z_+^{(n)} = 2nd + z_0 - z$ and $z_-^{(n)} = 2(n+1)d - z_0 - z$ the near-field dyadic Green's function for $\mathbf{r} \in 3$ may be expressed as

$$\mathbf{G}_3^{\text{nf}}(\mathbf{r}, \mathbf{r}_0) = \frac{1 - \beta_3}{4\pi k_3^2} \sum_{n=0}^{\infty} (\beta_2\beta_3)^n \{[\Gamma_1(\rho, z_+^{(n)}) - \beta_2\Gamma_1(\rho, z_-^{(n)})]\hat{z}\hat{z} + [\Gamma_2(\rho, z_+^{(n)}) - \beta_2\Gamma_2(\rho, z_-^{(n)})]\hat{\rho}\hat{z}$$
$$+ [\Gamma_3(\rho, z_+^{(n)}) + \beta_2\Gamma_3(\rho, z_-^{(n)})]\hat{\rho}\hat{\rho} + [\Gamma_4(\rho, z_+^{(n)}) + \beta_2\Gamma_4(\rho, z_-^{(n)})]\hat{\varphi}\hat{\varphi} + [\Gamma_2(\rho, z_+^{(n)}) + \beta_2\Gamma_2(\rho, z_-^{(n)})]\hat{z}\hat{\rho}\}. \quad (23)$$

The z dependence of the near-field intensity in the substrate can be investigated as

$$\frac{dP_3^{\text{nf}}}{dz} = \int_0^{2\pi} \int_0^{\infty} \rho \, d\rho \, d\varphi \, |\mathbf{E}_3^{\text{nf}}(\mathbf{r})|^2, \quad (24)$$

where $\mathbf{E}_3^{\text{nf}}(\mathbf{r})$ is calculated from Eq. (1) using the near-field dyadic Green's function of Eq. (23). The imaginary part of ε_3 is obviously essential for the absorption process. However, as $\text{Im}\varepsilon_3 \ll \text{Re}\varepsilon_3$ the effect of $\text{Im}\varepsilon_3$ on the near-field itself is negligible. Hence, $\mathbf{E}_3^{\text{nf}}(\mathbf{r})$ can be evaluated under the assumption that ε_3 (β_3) is real. Thus by ignoring the small imaginary part of ε_3 we obtain for a vertical dipole emitter

$$\frac{dP_3^{(v),\text{nf}}}{dz} = I_0 d^4 \sum_{n,m=0}^{\infty} (\beta_2\beta_3)^{n+m} \left\{ \frac{1}{(z_+^{(n)} + z_+^{(m)})^4} + \frac{\beta_2^2}{(z_-^{(n)} + z_-^{(m)})^4} - \frac{2\beta_2}{(z_+^{(n)} + z_-^{(m)})^4} \right\}, \quad (25)$$

where $I_0 = 6|p_0|^2/(\pi \varepsilon_0^2 |\varepsilon_1 + \varepsilon_3|^2 d^4)$. Similarly, for a horizontal dipole emitter we obtain

$$\frac{dP_3^{(h),\text{nf}}}{dz} = \frac{1}{2} I_0 d^4 \sum_{n,m=0}^{\infty} (\beta_2\beta_3)^{n+m} \left\{ \frac{1}{(z_+^{(n)} + z_+^{(m)})^4} + \frac{\beta_2^2}{(z_-^{(n)} + z_-^{(m)})^4} + \frac{2\beta_2}{(z_+^{(n)} + z_-^{(m)})^4} \right\}. \quad (26)$$

The total near-field power absorbed in the silicon substrate can be calculated as

$$P_{\text{abs}}^{(v,h),\text{nf}} = \frac{\varepsilon_0\omega}{2} \text{Im}\varepsilon_3 \int_{-\infty}^{0} dz \frac{dP_3^{(v,h),\text{nf}}}{dz}. \quad (27)$$

This yields

$$P_{\text{abs}}^{(v,h),\text{nf}} = \frac{3 \pm 1}{4} \frac{\omega \text{Im}\varepsilon_3 |p_0|^2}{16\pi\varepsilon_0 |\varepsilon_1 + \varepsilon_3|^2} \sum_{n,m=0}^{\infty} (\beta_2\beta_3)^{n+m} \left\{ \frac{1}{[d(n+m) + z_0]^3} + \frac{\beta_2^2}{[d(n+m+2) - z_0]^3} \mp \frac{2\beta_2}{[d(n+m+1)]^3} \right\}, \quad (28)$$

where the upper and lower signs are used for vertical and horizontal dipoles, respectively. Eq. (28) is an expression for the total near-field absorption in the substrate. In principle this expression is singular for $n = m = 0$ if the dipole is positioned directly at the substrate surface, where $z_0 = 0$. However, if a small particle is positioned exactly at $z_0 = 0$ the dipole approximation becomes inadequate, as it is only an infinitesimal part of the particle that would lie at a distance $z_0 \approx 0$. In this case one would have to divide the particle into many pieces with different distances to the surface and then make a summation. For a small spherical particle this effectively corresponds to a dipole emitter at a distance $z_0 \approx r$, where r is the radius of the small sphere. Thus Eq. (28) is, strictly speaking, not valid for dipoles at $z_0 = 0$. Furthermore, the dipole moment p_0 of such a dipole would roughly be proportional to z_0^3, in which case Eq. (28) does not become singular as z_0 approaches 0.

III. RESULTS

Utilizing the dyadic Green's function approach of Sec. II, we analyze near- and far-field radiation from an electric point dipole (which represents a small metal scatterer) embedded within a high refractive index layer of rutile TiO$_2$ on top of a silicon surface. We will start by investigating the z dependence of the near-field intensity in the silicon substrate for a dipole emitter placed in the middle of the thin rutile film $z_0 = d/2$. This can be done by evaluating the double sums in Eqs. (25) and (26) (due to the rapid convergence, numerically the sums are terminated at $n = m = 5$). The result is illustrated in Fig. 4 using log scales for both the x and y axes. The figure shows how the near-field intensity in the silicon substrate decreases rapidly and approaches a $|z|^{-4}$ behavior asymptotically when $|z|$ increases (the two dashed lines have a slope of -4). At a distance $|z| = d$ from the surface dP_3^{nf}/dz is below 0.01 in units of I_0 for both polarizations.

Now we wish to demonstrate numerically how the near- and far-field approximations of the dyadic Green's function can be utilized to approximate the electric field in the two limits and we wish to study the importance of near-field absorption. In order to calculate the absorption we use complex refractive indices for the silicon substrate taken from Ref. 36. As an example consider a vertical dipole situated at $z_0 = 10$ nm in a film of thickness $d = 20$ nm. In Fig. 5 we illustrate the radial
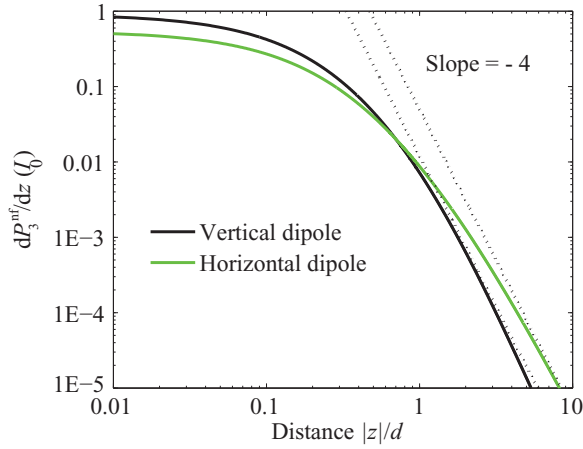
FIG. 4. (Color online) Distance dependence of the near-field intensity in the silicon ($\varepsilon_3 = 12$) substrate of a dipole emitter placed in $z_0 = d/2$ in a rutile TiO$_2$ ($\varepsilon_1 = 6.25$) film of thickness d. The medium above the film is air ($\varepsilon_2 = 1$). Both a vertical and a horizontal dipole emitter is considered.

dependence of the z component of the electric field within the silicon substrate at a fixed propagation angle $\theta = \pi/4$. The black curve is calculated using the $\hat{z}\hat{z}$ component of the full dyadic Green's function in Eq. (7), where the integral is calculated numerically using a 5000-point Gauss-Legendre quadrature that is cut at a value of κ_ρ/k_0 of at least 1500. The other curve is the sum of the z component of the field calculated using the near- and far-field approximation of the dyadic Green's function, Eqs. (14) and (23), respectively. It is seen that a good correspondence is found both in the near and the far field, and that a deviation is present in the intermediate region. Note also that the field is large and rapidly decaying in the near field (a log scale is used on the y axis). As we intend to utilize the far-field approach presented in Secs. II B and II C to study in detail the directionality of the radiation from the dipole
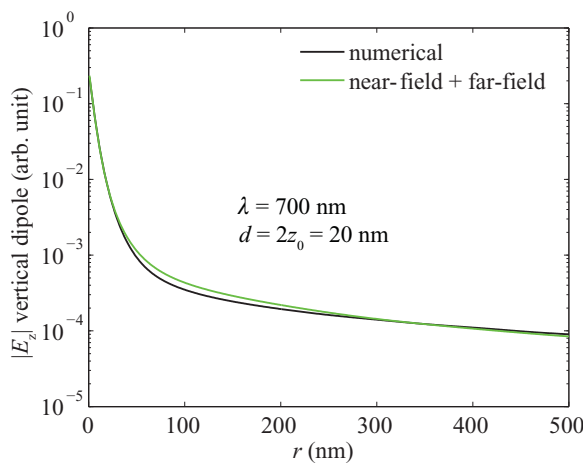
FIG. 5. (Color online) Radial dependence of the z component of the electric field within the silicon substrate for a vertical dipole. The angle θ is fixed at $\pi/4$ and the complex refractive index of silicon is taken from Ref. 36 ($n_{\rm si} = 3.78 + 0.0126i$ at $\lambda = 700$ nm). The refractive indices of the rutile film and the air superstrate are fixed at 2.5 and 1, respectively. The film thickness is taken to be $d = 20$ nm and z_0 is $d/2$.
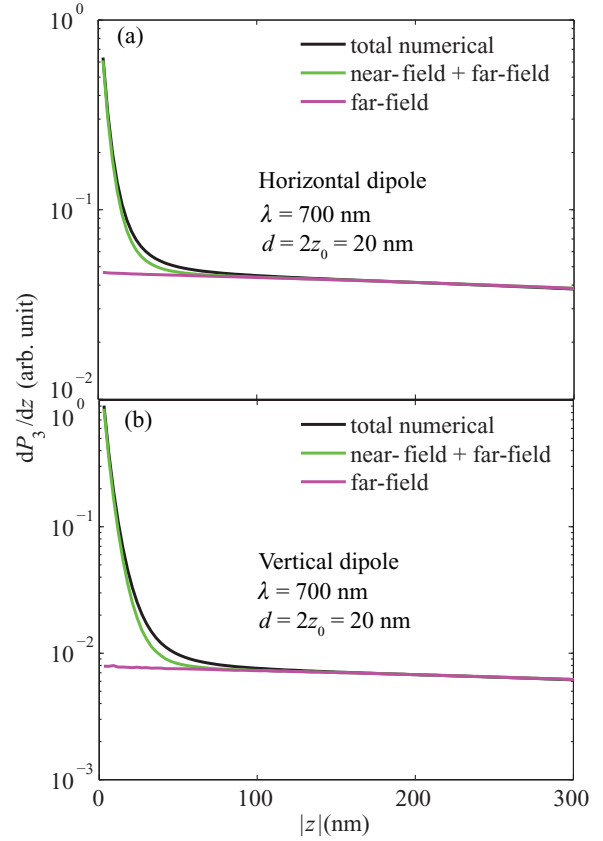
FIG. 6. (Color online) z dependence of the intensity within the silicon substrate. For details of the parameters see the caption to Fig. 5. (a) Horizontal dipole; (b) vertical dipole.

emitter we first investigate to what extent near-field absorption in the silicon substrate is important. This is done by integrating the modulus of the field squared over the entire absorbing silicon substrate. By doing this using both the total field and the near-field approximation, the amount of near-field power absorbed can readily be calculated as $P_{\rm abs}^{\rm nf}/P_{\rm abs}$, where $P_{\rm abs}$ is the total power absorbed in the silicon substrate calculated using the full dyadic Green's function. The z dependence of the intensity in the silicon substrate has been calculated using the full dyadic Green's function, the near-field approximation, and the far-field approximation (Fig. 6). Results are presented both for a horizontal and a vertical dipole emitter. Note again how the two approximations fit the full calculation in the two limits. By integrating the different curves in Fig. 6 from $z = 0$ to $-\infty$ both the total and the near-field absorption can be estimated. In the far-field analysis we have chosen to fix the wavelength at 700 nm and to investigate two different configurations in detail: one where the rutile film thickness is equal to the free space wavelength $d = \lambda$ and one where the thickness of the film is $d = \lambda/10$. At a wavelength of 700 nm using $n_{\rm si} = 3.78 + 0.0126i$ (taken from Ref. 36) we find for $d = \lambda$ and $d = \lambda/10$ that the amount of absorption that takes place in the near-field is relatively small, in particular if the dipole emitter is not very close (within 5 nm) to the silicon surface. For instance, for $z_0 = 10$ nm and $d = 70$ nm the near-field absorption is below 6% for a vertical dipole emitter and below 4% for a horizontal one. In order to get significant near-field

absorption the most important parameter is z_0. If z_0 is reduced to 5 nm the near-field absorption increases substantially. For a vertical dipole emitter we find that close to 30% of the power is absorbed in the near field and for a horizontal one we find 23%. Also the film thickness d and the wavelength λ have influence on the near-field absorption. If we reduce d to 10 nm, keeping $z_0 = 5$ nm and $\lambda = 700$ nm the near-field absorption accounts for 83% (23%) of the total absorption for a vertical (horizontal) dipole emitter. At wavelength of 400 nm, where $n_{si} = 5.57 + 0.387i$ (Ref. 36), with $d = 2z_0 = 10$ nm we find for a vertical dipole that close to 80% of the power is absorbed in the near field and for a horizontal dipole we find 38%. However, for the two configurations chosen for the far-field analysis ($\lambda = 700$ nm and $d = \lambda$ or $\lambda/10$) we have found that near-field absorption is quite small, especially if $z_0 > 5$ nm. Near-field absorption can, therefore, to a good approximation be neglected, and we find it reasonable to use an approach that relies on far fields only.

To evaluate the directionality of the radiation from the point dipole we utilize the far-field approach outlined in Secs. II B and II C. Because we take the far-field approach the silicon substrate will in all what follows be modeled as a lossless dispersionless dielectric with a dielectric constant of 12. First we display the angular distribution of the scattered power using the integral kernels together with the square root front factors of Eqs. (17) and (18). In the first configuration, where $d = \lambda$, the radiation pattern of a dipole embedded within the rutile film at $z_0 = 350$ nm shows that the scattered light with a very strong preference is directed into the silicon, the radiation pattern in the air above the rutile film is not noticeable (Fig. 7). Within the silicon we see that light is primarily refracted under an angle below but very close to the critical angle θ_c which separates the regions of allowed (coming from propagating waves within the rutile) and forbidden (coming from evanescent waves within the rutile film) light within the silicon. The boundaries between the allowed and forbidden regions in the silicon are depicted in the figure with two straight dotted lines.
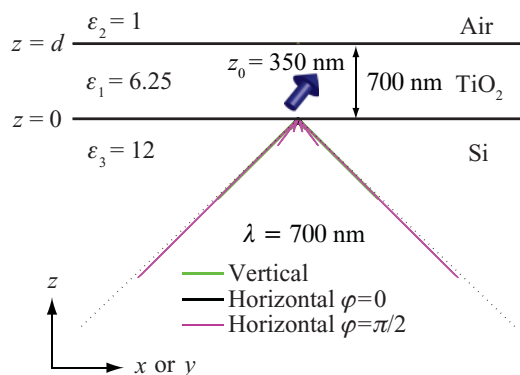
FIG. 7. (Color online) Angular radiation pattern of a vertical (solid green) and a horizontal (solid black line for $\varphi = 0$ and dashed magenta line for $\varphi = \pi/2$ electric point dipole embedded within a $d = 700$ nm thin film of rutile TiO$_2$ ($\varepsilon_1 = 6.25$) on top of silicon ($\varepsilon_3 = 12$). The medium above the film is air ($\varepsilon_2 = 1$), the free space wavelength is 700 nm, and the point dipole is located in the center of the film at $z_0 = \lambda/2 = 350$ nm. The straight dotted black lines within the silicon are the boundaries between allowed (below the lines) and forbidden (above the lines) light.
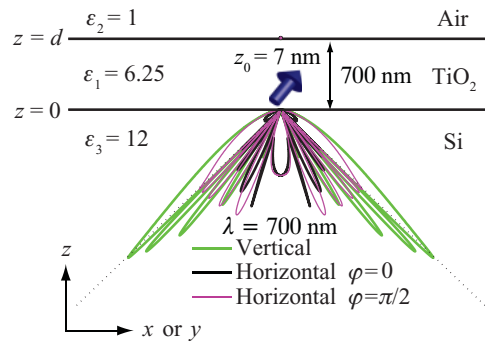
FIG. 8. (Color online) The same as Fig. 7, except $z_0 = \lambda/100 = 7$ nm.

Propagating light with the largest parallel momentum in the rutile film is directed parallel to the silicon surface and will couple into the silicon under an angle with respect to the surface normal of $\theta_c = \arcsin(\sqrt{\varepsilon_1/\varepsilon_3}) = 46.2°$. Thus light in the forbidden zone within the silicon (above the dotted straight lines) can only come from scattered waves which in the rutile film have $\kappa_\rho > k_1$ meaning that these waves are evanescent with κ_{z_1} imaginary. That κ_{z_1} becomes imaginary for large angles within the silicon is easily seen from $\kappa_{z_1} = k_1\sqrt{1 - \sin^2\theta\varepsilon_3/\varepsilon_1}$ as ε_3 is larger than ε_1. Evanescent waves are strong in the near field of the scatterer and can therefore contribute to the radiation distribution in the silicon if the scatterer is close to the surface.25 This can be seen from the results presented in Fig. 8. Here the angular radiation pattern of an electric point dipole is displayed for a dipole-surface separation of $z_0 = \lambda/100 = 7$ nm. The pattern clearly shows how a large part of the light is scattered into propagating waves within the forbidden zone in the silicon. Thus for a particle close to the silicon surface ($\lambda/100$) a significant part of the scattered evanescent near field can be coupled into propagating waves within the silicon. With thin-film silicon solar cells in mind this could be very important because if we assume an ideal rear reflector, the propagating waves in the forbidden zone will be completely trapped within the silicon film due to total internal reflection (they are propagating at angles larger than θ_c). Thus these waves will experience an infinite path length and will eventually be absorbed within the silicon. Note also again that a very little part of the radiation is scattered into the air above the rutile film.

For the second case where the film thickness is reduced to $d = \lambda/10 = 70$ nm and the dipole emitter is located in the center of the film the angular distribution of the scattered power is presented in Fig. 9. In this case the angle distribution is wider than for the thicker film (compare with Fig. 7), and it can be seen how also some of the scattered evanescent waves in the rutile, even for a dipole in the middle of the film, contribute to the propagating radiation in the silicon. For $d = 70$ nm and a dipole emitter close to the silicon surface $z_0 = 7$ nm the radiation pattern is depicted in Fig. 10. It can be seen how a large part of the scattered evanescent waves within the rutile film contribute to the propagating light within the silicon. When compared to Fig. 9 it is clear that a larger part of the radiation is located in the forbidden zone of the silicon.
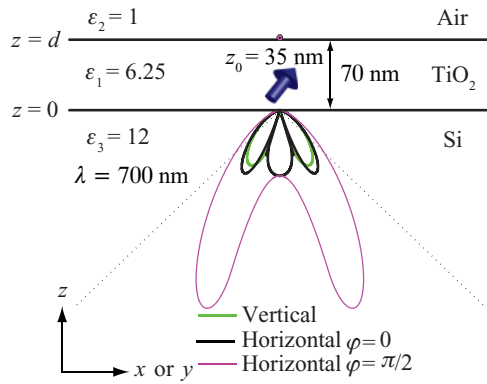
FIG. 9. (Color online) The same as Fig. 7, except $d = 70$ nm and $z_0 = 35$ nm.

For solar cells it is of course very important that the fraction of scattered light that couples into the silicon is as large as possible. From Figs. 7–10 it is clear that the radiation of the dipole emitter with a strong preference is directed toward the silicon. The explanation for this is that the silicon has a much higher refractive index than the rutile film and the air above has a much lower refractive index. By performing the integrals in Eqs. (17) and (18) it is possible to make an exact evaluation of the total amount of light scattered into the silicon σ_3 and into the air σ_2, respectively. We have evaluated σ_3/σ_2 versus the position of the dipole emitter z_0 for both film thicknesses; $d = \lambda$ (Fig. 11) and $d = \lambda/10$ (Fig. 12). Both horizontal and vertical dipole emitters are considered. From Fig. 11 it can be seen that scattering into the silicon dominates for both polarizations and for all positions of the dipole emitter. For a vertically polarized dipole emitter the ratio is much larger than for a horizontally polarized dipole. This is because a vertical dipole primarily radiates in the directions parallel to the interfaces whereas a horizontal dipole primarily radiates in the direction perpendicular to the interface. Thus most of the radiation from a vertical dipole will be incident on the rutile-air interface under an angle larger than the critical angle and will therefore experience total internal reflection. This is not the case for a horizontally polarized dipole emitter. Note that the ratio σ_3/σ_2 shows an interference phenomenon with a close to constant period not far from half the wavelength of
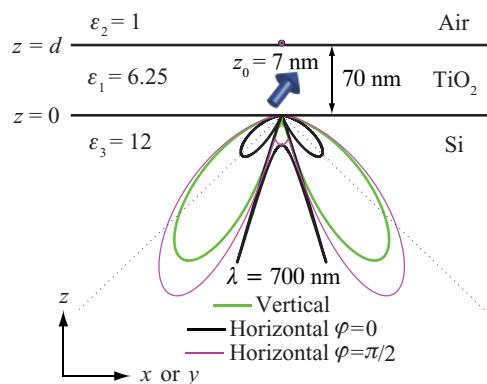
FIG. 10. (Color online) The same as Fig. 7, except $d = 70$ nm and $z_0 = 7$ nm.
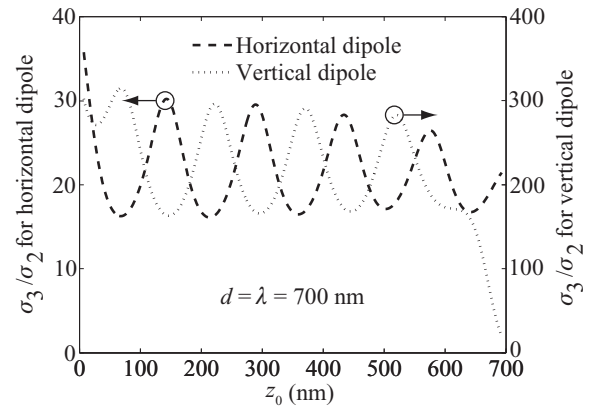
FIG. 11. Ratio between the total amount of light scattered into the silicon below and the air above the rutile film vs the position of the dipole emitter z_0. The film thickness is equal to the wavelength $d = \lambda = 700$ nm. The left y axis is for horizontally polarized dipoles and the right y axis is for vertically polarized dipoles.

the light in the rutile $\lambda/(2\sqrt{\varepsilon_1}) = 140$ nm. The interference phenomenon can also be seen from the radiation pattern in Fig. 8 where the scattering cross section is oscillating along θ. For plasmon assisted solar cells it is primarily the horizontally polarized dipole moments that are important, because under normal incidence, which is appropriate for solar cells, vertical dipole moments cannot be induced in the metal nanoparticles by the incident solar radiation. For horizontally polarized dipole emitters close to the silicon surface σ_3/σ_2 becomes larger than 30 meaning that more than 96% of the scattered radiation will couple into the silicon. For the thin film σ_3/σ_2 versus the position of the dipole emitter is presented in Fig. 12. In this case the interference phenomenon disappears because the film thickness is smaller than half the wavelength of the light in the rutile film. However, the results show that it is still possible to achieve a ratio larger than 30 for a horizontal dipole emitter if it is close to the silicon surface.

In order to estimate the path length enhancement and hence the absorption enhancement in the silicon due to the presence
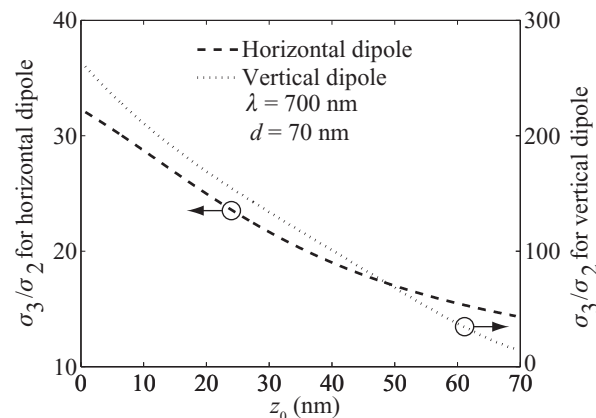
FIG. 12. Ratio between the total amount of light scattered into the silicon below and the air above the rutile film vs the position of the dipole emitter z_0. The film thickness is one tenth of the wavelength $d = \lambda/10 = 70$ nm.
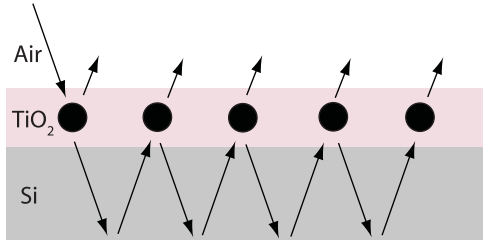
FIG. 13. (Color online) Schematic illustration of the multiple scattering events in the plasmon assisted thin-film Si solar cell under consideration.

of metal nanoscatterers within the rutile film we follow the approach of Catchpole and Polman in Ref. 6. The maximum path length enhancement L_{max} depends on multiple scattering events where the light is scattered via the embedded metal nanoparticles as illustrated schematically in Fig. 13. If we assume that the light is perfectly reflected at the rear side of the silicon film, the maximum path length enhancement can approximately be calculated as[6]

$$L_{max} = \frac{2d_{av}}{1 - f_{subs}}, \quad (29)$$

where d_{av} is the ratio of the path length of a single pass over the active silicon layer to its thickness averaged over the angular radiation distribution of the scattered power within the silicon and f_{subs} is the ratio of the power scattered into the silicon to the total scattered power in a single scattering event. Hence, L_{max} expresses the maximum path length enhancement (due to the presence of the nanoparticles) compared to a single pass across the active silicon layer. Thus if L_{max}, for example, is 50 and the thickness of the silicon film is 2 μm, then the maximum optical path length within the active silicon is approximately 100 μm. It should however be noted that the light that couples into the silicon in the forbidden zone (due to near-field coupling) will be perfectly reflected when it returns to the silicon-rutile interface, meaning that this part of the radiation will be completely trapped within the active silicon film. We calculate d_{av} by integrating the normalized angular distribution of the radiated power within the silicon weighted by $1/\cos\theta$, thus

$$d_{av} = \frac{\int_0^{2\pi} \int_0^{\frac{\pi}{2}} r^2 \sin\theta d\theta d\varphi \frac{1}{\cos\theta} \langle \mathbf{S}_3 \rangle \cdot \hat{r}}{\int_0^{2\pi} \int_0^{\frac{\pi}{2}} r^2 \sin\theta d\theta d\varphi \langle \mathbf{S}_3 \rangle \cdot \hat{r}}, \quad (30)$$

where θ is defined as depicted in Fig. 2(a). f_{subs} is calculated as

$$f_{subs} = \frac{\sigma_3}{\sigma_2 + \sigma_3}, \quad (31)$$

where we assume that all the scattered light eventually will be coupled out of the rutile film.

For both polarizations of the emitter d_{av} and L_{max} have been calculated versus the position z_0 for the thick $d = \lambda = 700$ nm rutile film (Fig. 14) and for the thin $d = \lambda/10 = 70$ nm rutile film (Fig. 15). From Fig. 14(a) it can be seen how the normalized average propagation distance both for a horizontal and a vertical dipole emitter increases when the emitter approaches the silicon surface. For intermediate positions it can be noted that d_{av} is slightly smaller than $\sqrt{2}$ which means
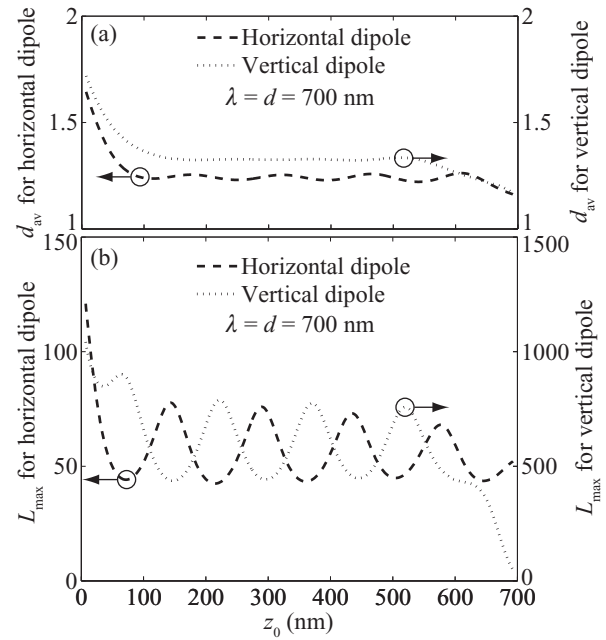
FIG. 14. (a) Normalized average propagation distance and (b) maximum path length enhancement vs the position of the dipole emitter z_0 for the configuration where $d = \lambda = 700$ nm.

that the average refraction angle is close to $45°$, which is in good agreement with the radiation distribution presented in Fig. 7. From the path length enhancements in Fig. 7(b) the interference phenomenon due to the thick film is clear. It can be noted that for a horizontal dipole an enhancement of over 100 can be achieved when the scatterer approaches the rutile-silicon interface. For intermediate distances the
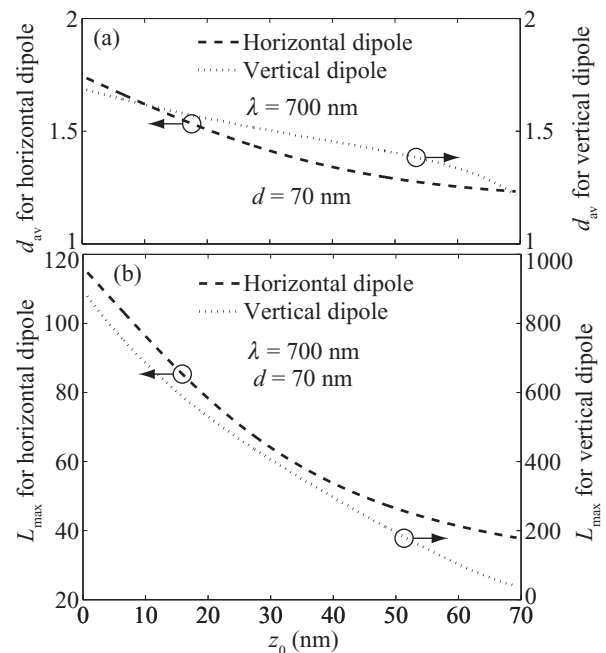
FIG. 15. (a) Normalized average propagation distance and (b) maximum path length enhancement vs the position of the dipole emitter z_0 for the configuration where $d = \lambda/10 = 70$ nm.
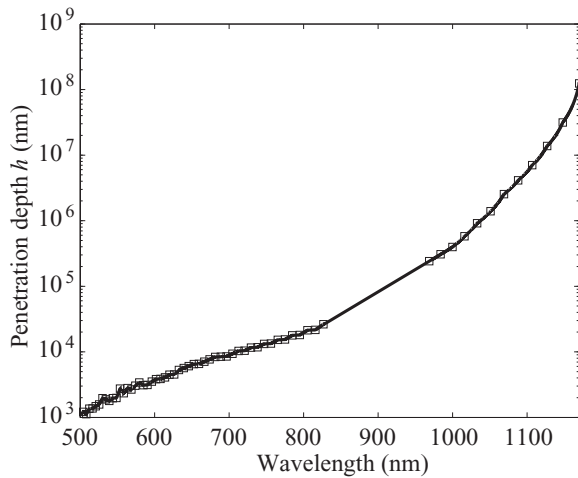
FIG. 16. Penetration depth of light in silicon vs the wavelength. The plot is based on experimental data taken from Palik (Ref. 36).

path length enhancement of a horizontal dipole oscillates around approximately 60. For vertically induced dipoles enhancements of over 1000 can even be achieved if the emitter is very close to the silicon surface. For the configuration where $d = \lambda/10 = 70$ nm d_{av} and L_{max} are presented versus the emitter position z_0 in Fig. 15. For both polarizations d_{av} decreases over the entire interval when z_0 increases. From the path length enhancements of Fig. 15(b), it can be seen how the thin-film configuration also allows for a path length enhancement of over 100 for horizontally induced dipole moments when the particle approaches the silicon surface.

To estimate how thick the silicon film must be in order to absorb the light the extinction coefficient (the imaginary part of the complex refractive index $\text{Im}[\sqrt{\varepsilon_{Si}(\omega)}]$) of silicon is a key parameter. Based on data from Palik[36] we have plotted the penetration depth $h = 1/(\text{Im}[\sqrt{\varepsilon_{Si}(\omega)}]k_0)$ as a function of the wavelength (Fig. 16). Note the logarithmic scale on the y axis. For example at a wavelength of 700 nm the penetration depth is approximately 8.9 μm, at 1000 nm it is 0.4 mm, and at 1100 nm it has increased to 0.56 cm. These numbers must
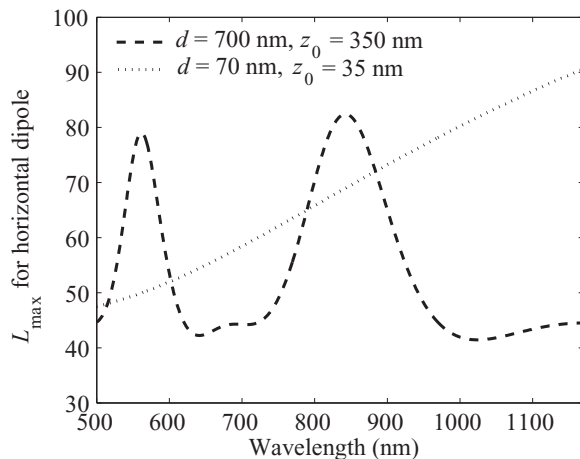
FIG. 17. Maximum path length enhancement L_{max} for horizontally polarized dipole moments as a function of the wavelength for $d = 700$ nm and $z_0 = 350$ nm (dashed curve) and for $d = 70$ nm and $z_0 = 35$ nm (dotted curve).

be compared to the maximum optical path length that can be achieved via the multiple scattering events in a plasmon assisted thin-film Si solar cell (cf. Fig. 13). Thus, in order to make the comparison we have calculated L_{max} as a function of the wavelength (Fig. 17). Only horizontally polarized dipole moments that are relevant in solar cell applications are considered. Based on the two different configurations analyzed above we have chosen to calculate L_{max} for $d = 700$ nm and $z_0 = 350$ nm (dashed curve), and for $d = 70$ nm and $z_0 = 35$ nm (dotted curve). In the configuration where the rutile film is 700 nm thick an oscillating behavior with a period that increases with the wavelength can be clearly seen. For the $d = 70$ nm configuration no oscillations are seen with the wavelength. At $\lambda = 700$ nm the configuration with the thin rutile film has $L_{max} \approx 60$ whereas the thick film configuration has $L_{max} \approx 45$. Thus for the optical path length to exceed the penetration depth at $\lambda = 700$ nm the thickness of the active Si film should at least be 8.9 μm/45 $\approx$ 200 nm. However, at longer wavelengths the required Si film thickness increases significantly. At $\lambda = 1000$ nm the Si film thickness should be a least 9.5 μm, and at $\lambda = 1100$ nm the required film thickness has increased to approximately 130 μm.

IV. CONCLUSION

Utilizing the dyadic Green's function formulation optimization and design of plasmon-assisted solar cell configurations have been analyzed. Metal nanoparticles embedded in high-index thin films placed on top of silicon solar cells are studied in the small particle limit, where only dipole contributions are important. Thus the metal nanoparticles are represented by electric point dipoles. Based on this assumption we have presented semianalytical expressions for light scattering both into the silicon substrate and into the air superstrate. These expressions are found by integrating the flux of the scattered power over semispheres in the sub- or superstrate, respectively. The flux of the scattered power is calculated exactly using analytical far-field approximations of the dyadic Green's function which have been derived from the full dyadic Green's function of the three-layer reference structure. Also a near-field approximation of the dyadic Green's function has been derived, which has been used to set up a semianalytical expression for the total near-field power absorbed in the substrate. Our theoretical approach has been used to analyze metal nanoscatterers within a thin rutile film on top of silicon. For a horizontal dipole emitter, which is the relevant polarization for solar cells, a fraction of more than 96% of the scattered radiation can be coupled into the silicon if the dipole is close to the silicon interface, and optical path length enhancements of more than 100 can be achieved.

APPENDIX A: ANGULAR INTEGRAL

The integral in Eq. (11) is evaluated using $k_i r \gg 1$ as follows:

$$\int_0^{\frac{\pi}{2}} d\alpha f(\alpha) \exp[ik_i r \cos(\alpha - \theta)]$$

$$= e^{ik_i r} \int_0^{\frac{\pi}{2}} d\alpha f(\alpha) \exp(ik_i r[\cos(\alpha - \theta) - 1])$$

$$\approx e^{ik_i r} f(\theta) \int_0^{\frac{\pi}{2}} d\alpha \exp\left(-i\frac{k_i r}{2}(\alpha - \theta)^2\right)$$

$$\approx e^{ik_i r} f(\theta) \int_{-\infty}^{\infty} d\Delta \exp\left(-i\frac{k_i r}{2}\Delta^2\right)$$

$$= f(\theta)\sqrt{\frac{2\pi}{ik_i r}} e^{ik_i r}, \tag{A1}$$

where $\Delta = \alpha - \theta$ and we have used that

$$\int_{-\infty}^{\infty} e^{-ax^2} dx = \sqrt{\frac{\pi}{a}}. \tag{A2}$$

APPENDIX B: FAR-FIELD APPROXIMATIONS: A SECOND APPROACH

In this approach we derive the far-field approximations of the dyadic Green's functions $\mathbf{G}_2^{(\mathrm{ff})}(\mathbf{r},\mathbf{r}')$ and $\mathbf{G}_3^{(\mathrm{ff})}(\mathbf{r},\mathbf{r}')$ starting from the dyadic Green's function of a homogenous material $\mathbf{G}_0(\mathbf{r},\mathbf{r}')$. In cylindrical coordinates (ρ,φ,z) $\mathbf{G}_0(\mathbf{r},\mathbf{r}')$ may be written as a Sommerfeld integral over the in-plane ($\perp$ to $\hat{z}$) momentum κ_ρ. We split into s- and p-polarized waves as $\mathbf{G}_0(\mathbf{r},\mathbf{r}') = \mathbf{G}_0^{(s)}(\mathbf{r},\mathbf{r}') + \mathbf{G}_0^{(p)}(\mathbf{r},\mathbf{r}')$ and get[37]

$$\mathbf{G}_0^{(s)}(\mathbf{r},\mathbf{r}') = \frac{-i}{4\pi} \int_0^\infty d\kappa_\rho \frac{e^{i\kappa_{z_1}|z-z'|}}{\kappa_{z_1}} \left[\frac{J_0'(\kappa_\rho\rho)}{\rho}\hat{\rho}\hat{\rho} + \kappa_\rho J_0''(\kappa_\rho\rho)\hat{\varphi}\hat{\varphi}\right], \tag{B1a}$$

$$\mathbf{G}_0^{(p)}(\mathbf{r},\mathbf{r}') = \frac{i}{4\pi k_1^2} \int_0^\infty d\kappa_\rho e^{i\kappa_{z_1}|z-z'|}\left[\frac{\kappa_\rho^3}{\kappa_{z_1}}J_0(\kappa_\rho\rho)\hat{z}\hat{z} + i\frac{z-z'}{|z-z'|}[\hat{\rho}\hat{z} + \hat{z}\hat{\rho}]\kappa_\rho^2 J_0'(\kappa_\rho\rho) - \kappa_{z_1}\kappa_\rho J_0''(\kappa_\rho\rho)\hat{\rho}\hat{\rho} - \kappa_{z_1}\frac{J_0'(\kappa_\rho\rho)}{\rho}\hat{\varphi}\hat{\varphi}\right], \tag{B1b}$$

where we have assumed that $\rho' = 0$. The derivation is presented for $\mathbf{r} \in 2$ to obtain $\mathbf{G}_2^{(\mathrm{ff})}(\mathbf{r},\mathbf{r}_0)$. For $\mathbf{r} \in 3$ a very similar derivation can be made to obtain $\mathbf{G}_3^{(\mathrm{ff})}(\mathbf{r},\mathbf{r}_0)$. We start with the s-polarized part of the dyadic Green's function. For a three-layer structure where the emitter is located within the thin film [see Fig. 2(b) and note that $z' = z_0$] the factor $e^{i\kappa_{z_1}|z-z'|}$ must be replaced as

$$e^{i\kappa_{z_1}|z-z'|} \rightarrow \left\{e^{i\kappa_{z_1}(d-z')}t_{12}^{(s)}\left[\sum_{n=0}^\infty \left(r_{12}^{(s)}r_{13}^{(s)}e^{2i\kappa_{z_1}d}\right)^n\right] + e^{i\kappa_{z_1}z'}r_{13}^{(s)}e^{i\kappa_{z_1}d}t_{12}^{(s)}\left[\sum_{n=0}^\infty \left(r_{12}^{(s)}r_{13}^{(s)}e^{2i\kappa_{z_1}d}\right)^n\right]\right\} e^{i\kappa_{z_2}(z-d)} = \xi_{+,2}^{(s)}(\kappa_\rho,z',d)e^{i\kappa_{z_2}z}. \tag{B2}$$

By substituting this into Eq. (B1a) an expression identical to Eq. (7a) is obtained. In the far field the κ_ρ integration limit is taken as k_2, and we may write $\kappa_\rho = k_2\sin\alpha$, $\kappa_{z_2} = k_2\cos\alpha$, $d\kappa_\rho = \kappa_{z_2}d\alpha$, and $k_2\sin\alpha = k_1\sin\alpha'$. Furthermore we introduce θ [see Fig. 2(b)] and get $z = r\cos\theta$ and $\rho = r\sin\theta$. As ρ is large the $\hat{\rho}\hat{\rho}$ term of the s-polarized part of the dyadic Green's function vanishes. If we, as in Sec. II, make an asymptotic expansion of the Bessel function for ρ large it is easy to see that we again encounter integrals like Eq. (11), and after some algebra the s-polarized part of the far-field approximation of $\mathbf{G}_2(\mathbf{r},\mathbf{r}')$ can be obtained as

$$\mathbf{G}_2^{(s,\mathrm{ff})}(\mathbf{r},\mathbf{r}_0) = \frac{e^{ik_2 r}}{4\pi r}\frac{\kappa_{z_2}}{\kappa_{z_1}}\xi_{+,2}^{(s)}(\theta,z_0,d)\hat{\varphi}\hat{\varphi}, \tag{B3}$$

where it is understood that $\kappa_{z_2} = k_2\cos\theta$, $\kappa_{z_1} = k_1\sqrt{1 - \sin^2\theta\,\varepsilon_2/\varepsilon_1}$, and $\kappa_{z_3} = k_3\sqrt{1 - \sin^2\theta\,\varepsilon_2/\varepsilon_3}$. For p polarization we first analyze the case of a z-oriented dipole. Starting from Eq. (B1b) this yields

$$\mathbf{G}_0^{(p)}(\mathbf{r},\mathbf{r}') \cdot \hat{z} = \frac{i}{4\pi k_1^2} \int_0^\infty d\kappa_\rho e^{i\kappa_{z_1}|z-z'|}$$

$$\times \left[\frac{\kappa_\rho^3}{\kappa_{z_1}}J_0(\kappa_\rho\rho)\hat{z} + i\frac{z-z'}{|z-z'|}\kappa_\rho^2 J_0'(\kappa_\rho\rho)\hat{\rho}\right]. \tag{B4}$$

For a three-layer structure where the emitter is located in medium 1 the p-polarized part transforms as $\hat{\rho} \rightarrow \hat{\rho}\frac{\kappa_{z_2}}{\kappa_{z_1}}$ and

$$e^{i\kappa_{z_1}|z-z'|} \rightarrow \left\{e^{i\kappa_{z_1}(d-z')}t_{12}^{(p)}\left[\sum_{n=0}^\infty \left(r_{12}^{(p)}r_{13}^{(p)}e^{2i\kappa_{z_1}d}\right)^n\right] + e^{i\kappa_{z_1}z'}r_{13}^{(p)}e^{i\kappa_{z_1}d}t_{12}^{(p)}\left[\sum_{n=0}^\infty \left(r_{12}^{(p)}r_{13}^{(p)}e^{2i\kappa_{z_1}d}\right)^n\right]\right\} \frac{\varepsilon_1}{\varepsilon_2}e^{i\kappa_{z_2}(z-d)}$$

$$= \xi_{+,2}^{(p)}(\kappa_\rho,z',d)\frac{\varepsilon_1}{\varepsilon_2}e^{i\kappa_{z_2}z}, \tag{B5}$$

where the factor $\varepsilon_1/\varepsilon_2$ must be introduced if $t_{12}^{(p)} = 1 + r_{12}^{(p)}$ and $r_{12}^{(p)}$ is given by Eq. (5). With the same arguments as above and after some algebra the far-field approximation becomes

$$\mathbf{G}_2^{(p,\mathrm{ff})}(\mathbf{r},\mathbf{r}_0) \cdot \hat{z} = -\frac{e^{ik_2 r}}{4\pi r} \sin\theta \frac{\kappa_{z_2}}{\kappa_{z_1}} \xi_{+,2}^{(p)}(\theta, z_0, d)\hat{\theta}, \quad \text{(B6)}$$

where again it is understood that $\kappa_{z_2} = k_2 \cos\theta$, $\kappa_{z_1} = k_1\sqrt{1 - \sin^2\theta \varepsilon_2/\varepsilon_1}$, and $\kappa_{z_3} = k_3\sqrt{1 - \sin^2\theta \varepsilon_2/\varepsilon_3}$.

For a ρ-oriented dipole Eq. (B1b) yields

$$\mathbf{G}_0^{(p)}(\mathbf{r},\mathbf{r}') \cdot \hat{\rho} = \frac{i}{4\pi k_1^2} \int_0^\infty d\kappa_\rho e^{i\kappa_{z_1}|z-z'|}$$
$$\times \left[-\kappa_\rho \kappa_{z_1} J_0''(\kappa_\rho)\hat{\rho} + i \frac{z-z'}{|z-z'|} \kappa_\rho^2 J_0'(\kappa_\rho \rho)\hat{z} \right] \quad \text{(B7)}$$

and in this case $\hat{\rho} \to \hat{\rho}\frac{\kappa_{z_2}}{\kappa_{z_1}}$ and the factor $e^{i\kappa_{z_1}|z-z'|}$ must be replaced as

$$e^{i\kappa_{z_1}|z-z'|} \to \left\{ e^{i\kappa_{z_1}(d-z')} t_{12}^{(p)} \left[\sum_{n=0}^\infty \left(r_{12}^{(p)} r_{13}^{(p)} e^{2i\kappa_{z_1}d}\right)^n \right] - e^{i\kappa_{z_1}z'} r_{13}^{(p)} e^{i\kappa_{z_1}d} t_{12}^{(p)} \left[\sum_{n=0}^\infty \left(r_{12}^{(p)} r_{13}^{(p)} e^{2i\kappa_{z_1}d}\right)^n \right] \right\} \frac{\varepsilon_1}{\varepsilon_2} e^{i\kappa_{z_2}(z-d)}$$
$$= \xi_{-,2}^{(p)}(\kappa_\rho, z', d) \frac{\varepsilon_1}{\varepsilon_2} e^{i\kappa_{z_2}z}, \quad \text{(B8)}$$

where it should be noted that the sign of the field changes after the reflection. In the far field we obtain

$$\mathbf{G}_2^{(p,\mathrm{ff})}(\mathbf{r},\mathbf{r}_0) \cdot \hat{\rho} = \frac{e^{ik_2 r}}{4\pi r} \cos\theta \xi_{-,2}^{(p)}(\theta, z_0, d)\hat{\theta}. \quad \text{(B9)}$$

Thus the entire far-field approximation of the dyadic Green's function for a dipole emitter in medium 1 and an observation point in the superstrate ($\mathbf{r} \in 2$) can be constructed from the combination of Eqs. (B3), (B6), and (B9) as

$$\mathbf{G}_2^{(\mathrm{ff})}(\mathbf{r},\mathbf{r}_0) = \frac{e^{ik_2 r}}{4\pi r} \left[\frac{\kappa_{z_2}}{\kappa_{z_1}} \xi_{+,2}^{(s)}(\theta, z_0, d)\hat{\varphi}\hat{\varphi} - \sin\theta \frac{\kappa_{z_2}}{\kappa_{z_1}} \xi_{+,2}^{(p)}(\theta, z_0, d)\hat{\theta}\hat{z} + \cos\theta \xi_{-,2}^{(p)}(\theta, z_0, d)\hat{\theta}\hat{\rho} \right], \quad \text{(B10)}$$

which is identical to Eq. (13) and where it should be noted that θ and $\hat{\theta}$ is defined as shown in Fig. 2(b). For $\mathbf{r} \in 3$ a similar derivation yields an expression identical to Eq. (14) with θ and $\hat{\theta}$ defined as depicted in Fig. 2(a).

*jung@nano.aau.dk

[1] S. Lal, S. Link, and N. J. Halas, Nature Photon. **1**, 641 (2007).

[2] W. A. Murray and W. L. Barnes, Adv. Mater. **19**, 3771 (2007).

[3] A. V. Zayats and I. I. Smolyaninov, J. Opt. A: Pure Appl. Opt. **5**, S16 (2003).

[4] S. A. Maier and H. A. Atwater, J. Appl. Phys. **98**, 011101 (2005).

[5] H. A. Atwater and A. Polman, Nature Mater. **9**, 205 (2010).

[6] K. R. Catchpole and A. Polman, Appl. Phys. Lett. **93**, 191113 (2008).

[7] K. R. Catchpole and A. Polman, Opt. Express **16**, 21793 (2008).

[8] H. R. Stuart and D. G. Hall, Appl. Phys. Lett. **69**, 2327 (1996).

[9] H. R. Stuart and D. G. Hall, Appl. Phys. Lett. **73**, 3815 (1998).

[10] D. M. Schaadt, B. Feng, and E. T. Yu, Appl. Phys. Lett. **86**, 063106 (2005).

[11] D. Derkacs, S. H. Lim, P. Matheu, W. Mar, and E. T. Yu, Appl. Phys. Lett. **89**, 093103 (2006).

[12] J. S. Biteen, N. S. Lewis, H. A. Atwater, H. Mertens, and A. Polman, Appl. Phys. Lett. **88**, 131109 (2006).

[13] S. Pillai, K. R. Catchpole, T. Trupke, and M. A. Green, J. Appl. Phys. **101**, 093105 (2007).

[14] C. F. Bohren and D. R. Huffman, *Absorption and Scattering of Light by Small Particles*, 1st ed. (Wiley & Sons, New York, 1983).

[15] J. Mertz, J. Opt. Soc. Am. B **17**, 1906 (2000).

[16] A. Taflove and S. Hagness, *Computational Electrodynamics: The Finite-Difference Time-Domain Method*, 3rd ed. (Artech House, Boston, 2005).

[17] C. T. Tai, *Dyadic Green's Functions in Electromagnetic Theory*, 1st ed. (Intext Educational Publishers, 1971).

[18] R. Chance, A. Prock, and R. Silbey, Adv. Chem. Phys. **37**, 1 (1978).

[19] J. S. Bagby and D. P. Nyquist, IEEE Trans. Microwave. Tech. **35**, 206 (1987).

[20] L. W. Li, J. A. Bennett, and P. L. Dyson, Int. J. Electron. **70**, 803 (1991).

[21] L. Novotny, B. Hecht, and D. W. Pohl, J. Appl. Phys. **81**, 1798 (1997).

[22] R. L. Hartman, S. M. Cohen, and P. T. Leung, J. Chem. Phys. **110**, 2189 (1999).

[23] R. L. Hartman, J. Opt. Soc. Am. A **17**, 1067 (2000).

[24] M. Paulus, P. Gay-Balmaz, and O. J. F. Martin, Phys. Rev. E **62**, 5797 (2000).

[25] L. Novotny and B. Hecht, *Principles of Nano-Optics*, 1st ed. (Cambridge University Press, Cambridge, United Kingdom, 2006).

[26] J. Jung, T. G. Pedersen, T. Søndergaard, K. Pedersen, A. N. Larsen, and B. B. Nielsen, Phys. Rev. B **81**, 125413 (2010).

[27] J. Jung, T. G. Pedersen, T. Søndergaard, K. Pedersen, A. N. Larsen, and B. B. Nielsen, Phys. Status Solidi RRL **4**, 292 (2010).

[28] S. R. J. Brueck, IEEE J. Sel. Top. Quantum Electron. **6**, 899 (2000).

[29] S. R. J. Brueck, V. A. Smagley, and P. G. Eliseev, Phys. Rev. E **68**, 036608 (2003).

[30] O. J. F. Martin, C. Girard, and A. Dereux, Phys. Rev. Lett. **74**, 526 (1995).

[31] J. P. Kottmann and O. J. F. Martin, IEEE T. Antenn. Propag. **48**, 1719 (2000).

[32] J. Jin, *The Finite Element Method in Electromagnetics*, 2nd ed. (Wiley, New York, 2002).

[33] T. Søndergaard, Phys. Status Solidi B **244**, 3448 (2007).

[34] J. Jung and T. Søndergaard, Phys. Rev. B **77**, 245310 (2008).

[35] A. M. Kern and O. J. F. Martin, J. Opt. Soc. Am A **26**, 732 (2009).

[36] E. D. Palik, *Handbook of Optical Constants of Solids*, 1st ed. (Academic Press, New York, 1985).

[37] T. Søndergaard and S. I. Bozhevolnyi, Phys. Rev. B **69**, 045422 (2004).